# Characterization of $Nd_{0.6}Sr_{0.4}Co_{1-y}Fe_yO_{3-\delta}$ $(0 \leq y \leq 0.5)$ cathode materials for intermediate temperature solid oxide fuel cells

K.T. Lee, A. Manthiram*

*Materials Science and Engineering Program, University of Texas at Austin, Austin, TX 78712, United States*

## Abstract

The crystal chemistry, electrical conductivity, thermal expansion behavior, chemical compatibility, and electrochemical performance of perovskite $Nd_{0.6}Sr_{0.4}Co_{1-y}Fe_yO_{3-\delta}$ $(0 \leq y \leq 0.5)$ oxides as cathode materials for intermediate temperature solid oxide fuel cells have been investigated. The samples crystallize in an orthorhombic structure, and the lattice parameters and cell volume increase with increasing Fe content $y$. The degree of oxygen loss on heating to higher temperatures and the thermal expansion coefficient (TEC) decrease with increasing $y$ due to a stronger Fe–O bond. The electrical conductivity decreases with $y$, and the system exhibits a metal to semiconductor transition at around $y = 0.2$. The electrocatalytic activity and power density measured with single cells decrease with increasing $y$ due to a decrease in electrical conductivity and oxide ion vacancy concentration.
© 2005 Elsevier B.V. All rights reserved.

*Keywords:* Solid oxide fuel cells; Crystal chemistry; Electrical conductivity; Thermal expansion; Electrochemical performance

## 1. Introduction

The focus of the solid oxide fuel cells (SOFC) is shifting in recent years towards operating them at intermediate temperatures of 500–800 °C with hydrocarbon fuels since the lower temperatures can minimize the problems associated with thermal expansion mismatch and chemical reactivity among the components. However, a major issue with the reduced operating temperature is the decrease in the catalytic activity of the cathode for oxygen reduction [1]. The state-of-the-art cathode material for high temperature (~1000 °C) operation is the $La_{1-x}Sr_xMnO_3$ perovskite oxide. However, its poor oxide ion conductivity prevents its use for intermediate temperature SOFC [2,3]. Development of alternative cathode materials with adequate mixed ionic–electronic conductivity (MIEC) is needed to make the intermediate temperature SOFC technology successful.

$La_{1-x}Sr_xCoO_{3-\delta}$ perovskite oxide is appealing in this regard as it exhibits high oxide ion conductivity due to a significant amount of oxide ion vacancies in the lattice at the intermediate operating temperatures of 500–800 °C. Its high ionic conductivity enables the migration of the oxygen species through the bulk as well as the surface of the electrode material to the three phase boundary (TPB) [4,5]. However, $La_{1-x}Sr_xCoO_{3-\delta}$ exhibits very large thermal expansion coefficient (TEC). Replacement of La by other smaller lanthanides could lower the thermal expansion due to the decreased ionicity of the Ln–O bond [6]. Accordingly, other Sr-doped lanthanide cobaltites $Ln_{1-x}Sr_xCoO_{3-\delta}$ (Ln=Pr, Nd, Sm, and Gd) have been investigated as cathode materials for intermediate temperature SOFC [7–11].

We showed previously that the $x = 0.4$ composition in the $Nd_{1-x}Sr_xCoO_{3-\delta}$ $(0 \leq x \leq 0.5)$ system exhibits the best electrochemical performance with adequate electronic conductivity [12]. Although the electrochemical performance of $Nd_{0.6}Sr_{0.4}CoO_{3-\delta}$ is satisfactory, it still has a larger TEC. With an aim to lower the TEC, we focus here on the synthesis and characterization of $Nd_{0.6}Sr_{0.4}Co_{1-y}Fe_yO_{3-\delta}$ $(0 \leq y \leq 0.5)$ cathodes; replacement of Co by Fe is known to

---

* Corresponding author. Tel.: +1 512 471 1791; fax: +1 512 471 7681.
  *E-mail address:* rmanth@mail.utexas.edu (A. Manthiram).

decrease the TEC, for example, in $La_{1-x}Sr_xCo_{1-y}Fe_yO_{3-\delta}$ [13–15]. The effect of Fe content on the crystal chemistry, electrical conductivity, thermal expansion, chemical compatibility, and electrochemical performance of the $Nd_{0.6}Sr_{0.4}Co_{1-y}Fe_yO_{3-\delta}$ cathodes is presented in this paper.

## 2. Experimental

The $Nd_{0.6}Sr_{0.4}Co_{1-y}Fe_yO_{3-\delta}$ compositions were synthesized by conventional solid state reaction. Required amounts of $Nd_2O_3$, $SrCO_3$, $Co_3O_4$, and $Fe_2O_3$ were fired in air first at 900 °C for 12 h, reground, pressed into pellets, and sintered at 1200 °C for 24 h. The sintering at 1200 °C was repeated for another 24 h after regrinding and repelletizing in order to improve the product homogeneity. The $La_{0.8}Sr_{0.2}Ga_{0.8}Mg_{0.2}O_{2.8}$ (LSGM) electrolyte was prepared by firing required amounts of $La_2O_3$, $SrCO_3$, $Ga_2O_3$, and $MgO$ at 1100 °C for 5 h, followed by pelletizing and sintering at 1500 °C for 10 h. $NiO–Ce_{0.9}Gd_{0.1}O_{1.95}$ (GDC) cermet (Ni:GDC=70:30 vol.%) anode was synthesized by the glycine–nitrate combustion method [16].

Crystal structural characterizations were carried out by analyzing the X-ray diffraction data with the Rietveld method. The average crystallite size was estimated from the line broadening in the X-ray diffraction patterns using the Scherrer equation [17],

$$\text{Crystallite size} = \frac{0.9\lambda}{\text{FW}\cdot\cos\theta} \qquad (1)$$

where $\lambda$ is the wavelength of the incident radiation and FW is the full width in radians at half maximum.

BET surface area was measured with a Quantachrom Autosorb-1 surface area and pore size analyzer. Thermogravimetric analysis (TGA) and thermal expansion data were collected with a Perkin-Elmer Series 7 thermal analysis system. TGA was carried out from room temperature to 1000 °C with a heating rate of 2 °C/min and a cooling rate of 10 °C/min in air. TECs of the sintered samples were measured from room temperature to 800 °C with a heating/cooling rate of 5 °C/min. Electrical conductivities of the sintered samples were measured in air with a four-probe dc method in the range of 200–900 °C with a heating rate of 5 °C/min by equilibrating for 30 min at each temperature before collecting the data. All the samples used for thermal expansion and conductivity measurements had densities of >95% of theoretical values.

Electrochemical performances were evaluated with single cells at 800 °C. The cathode and anode mixtures were obtained by ball-milling the $Nd_{0.6}Sr_{0.4}Co_{1-y}Fe_yO_{3-\delta}$ cathode and NiO–GDC cermet anode powders for 24 h in ethanol using a zirconia grinding media and mixing with a 40 wt.% organic binder (Heraeus V006). The cathodes and anodes were then fabricated by screen printing onto 0.8 mm thick LSGM electrolyte pellet, followed by firing for 3 h at 1000 °C for the cathode and 1200 °C for the anode. The
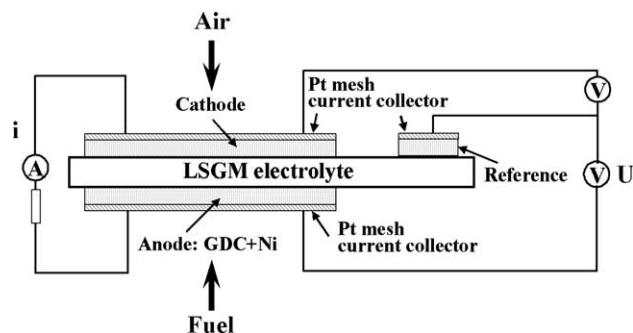


Fig. 1. Schematic configuration of the test single cell.

geometrical area of the electrode was 0.25 cm$^2$. Fig. 1 shows the schematic configuration of the test cell. Pt mesh was attached to the top of the electrodes as a current collector and Pt wire was used as terminals. In order to keep the current collector and electrode in good contact, a spring was used to press the Pt mesh onto the electrode via a porous alumina disk. Pt paste was used as the reference electrode on the cathode side. Humidified $H_2$ (~3% $H_2O$ at 30 °C) and air were supplied as fuel and oxidant, respectively, at a rate of 100 cm$^3$/min. NiO in the anode was reduced to Ni in humidified $H_2$ before the single cell test. $I–V$ and cathode over-potentials were measured in situ during cell operation with an Arbin BT2000 battery/fuel cell test station.

## 3. Results and discussion

### 3.1. Crystal chemistry and thermogravimetric analysis

X-ray diffraction indicated all the samples to be single phase and the patterns could be indexed on the basis of an orthorhombic perovskite ($GdFeO_3$ type) structure. The lattice parameters and the lattice volume increase with increasing Fe content $y$ (Fig. 2) due to the replacement of the smaller $Co^{3+}$($r=0.545$ Å) or $Co^{4+}$($r=0.530$ Å) ions by the larger $Fe^{3+}$($r=0.645$ Å) or $Fe^{4+}$($r=0.585$ Å) ions [18].

The TGA data of the various samples are shown in Fig. 3. The absence of hysteresis between the heating and cooling curves indicated that the oxygen contents are close to their equilibrium values at different temperatures during the TGA runs. Unfortunately, the absolute oxygen stoichiometry $(3-\delta)$ of the $Nd_{0.6}Sr_{0.4}Co_{1-y}Fe_yO_{3-\delta}$ samples at room temperature could not be determined precisely as the samples were hardly soluble in weakly acidic solutions to be analyzed by redox chemical titrations. Nevertheless, the relative degree of oxygen loss from the lattice could be clearly assessed with the TGA curves. The data in Fig. 3 reveal that the degree of oxygen loss decreases with increasing Fe content. Tai et al. [13] and Stevenson et al. [14] have also reported a similar trend for the analogous $La_{1-x}Sr_xCo_{1-y}Fe_yO_3$ system. The decrease in oxygen loss with Fe doping suggests a stronger binding of the oxygen to the lattice with increasing Fe. This is consistent with a
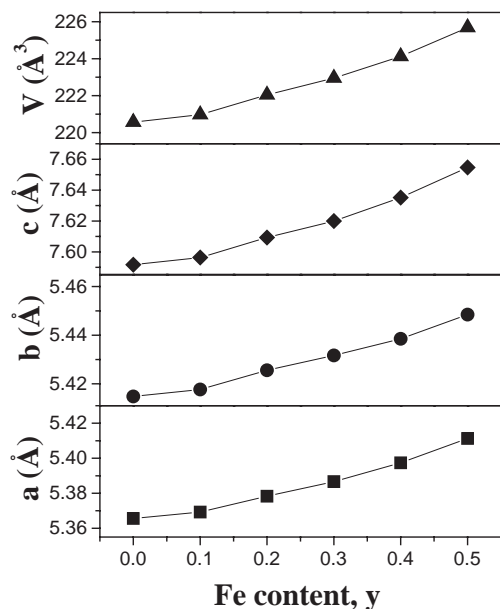
Fig. 2. Variations of the lattice parameters and lattice volume ($V$) of $Nd_{0.6}Sr_{0.4}Co_{1-y}Fe_yO_{3-\delta}$ with Fe content $y$.



Fig. 4. Variations of the electrical conductivity measured in air of $Nd_{0.6}Sr_{0.4}Co_{1-y}Fe_yO_{3-\delta}$ with temperature for various values of $y$.

higher standard Gibbs free energy of formation for $Fe_3O_4$ ($-1017.438$ kJ/mol) compared to that for $Co_3O_4$ ($-794.871$ kJ/mol) [19], implying a stronger Fe–O bond compared to the Co–O bond. It is also in accordance with the finding that the oxygen nonstoichiometry ($\delta$) of $La_{1-x}Sr_xFeO_{3-\delta}$ is almost fixed at $\delta \approx 0.5x$ over a wide range of $pO_2$, while the oxygen nonstoichiometry of $La_{1-x}Sr_xCoO_{3-\delta}$ increases with decreasing $pO_2$ [20].

## 3.2. Electrical conductivity and thermal expansion

The temperature dependence of the electrical conductivity of the $Nd_{0.6}Sr_{0.4}Co_{1-y}Fe_yO_{3-\delta}$ samples is shown in Fig. 4. A significant decrease in conductivity at higher temperatures could be due to the oxygen loss from the lattice at
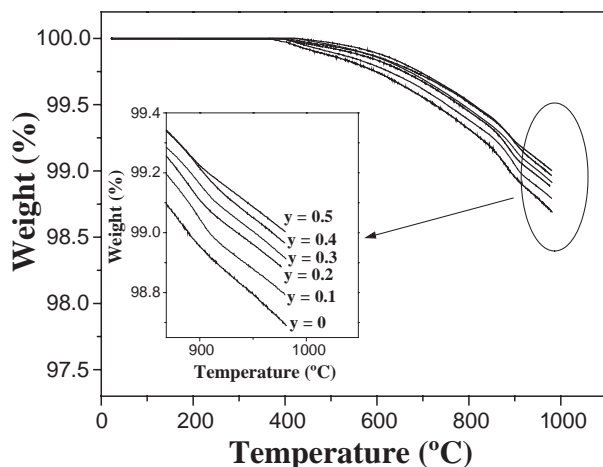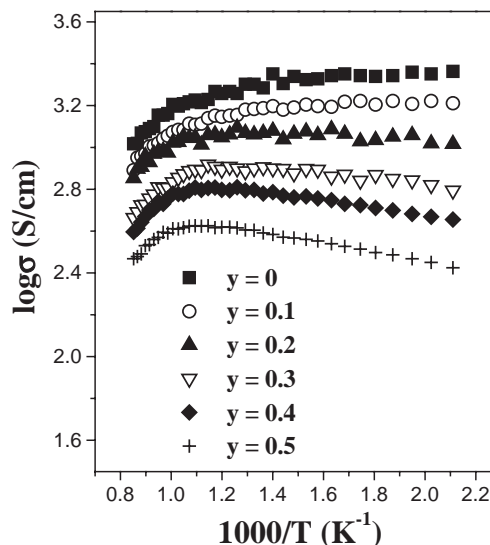


Fig. 3. TGA plots of $Nd_{0.6}Sr_{0.4}Co_{1-y}Fe_yO_{3-\delta}$ recorded in air with a heating rate of 2 °C/min.

higher temperatures as indicated by the TGA data (Fig. 3). The formation of oxide ion vacancies can, not only decrease the carrier concentration, but also perturb the (Co,Fe)–O–(Co,Fe) periodic potential and introduce carrier localization.

At a given temperature, the electrical conductivity decreases monotonically with increasing Fe doping. This is consistent with the fact that the conductivity of the end member $Nd_{0.6}Sr_{0.4}FeO_{3-\delta}$ (semiconductor) is about two orders of magnitude lower than that of the other end member $Nd_{0.6}Sr_{0.4}CoO_{3-\delta}$ (metallic) [12,21]. $Nd_{0.6}Sr_{0.4}Co_{1-y}Fe_yO_{3-\delta}$ is a mixed hopping conductor with more than one type of transition metal ions. It has been reported that the average valency of Fe is higher than that of Co in the analogous $La_{0.6}Sr_{0.4}Co_{1-y}Fe_yO_{3-\delta}$ system [22]. This suggests that the electronic charge compensation occurs preferentially by the formation of $Fe^{4+}$ rather than $Co^{4+}$ on substituting $Sr^{2+}$ for $Nd^{3+}$ in $Nd_{0.6}Sr_{0.4}Co_{1-y}Fe_yO_{3-\delta}$. Thus the preferential formation of $Fe^{4+}$ compared to $Co^{4+}$ and the decreased covalency of the $Fe^{4+}$–O bond compared to the $Co^{4+}$–O bond result in an increase in the electron localization and a decrease in the electrical conductivity with increasing Fe content.

The $Nd_{0.6}Sr_{0.4}Co_{1-y}Fe_yO_{3-\delta}$ system exhibits a metal to semiconductor transition around $y=0.2$ as seen in Fig. 4. As described previously with the $Nd_{1-x}Sr_xCoO_{3-\delta}$ system [12], the metal to semiconductor transition in $Nd_{0.6}Sr_{0.4}Co_{1-y}Fe_yO_{3-\delta}$ with Fe doping could be understood by considering the changes in the structural parameters. The end member $Nd_{0.6}Sr_{0.4}CoO_{3-\delta}$ is a metallic conductor with sufficient bandwidth and little or no charge transfer gap. A decrease in the tolerance factor $t$ as the smaller $Co^{3+}$ ions are replaced by the larger $Fe^{3+}$ ions in $Nd_{0.6}Sr_{0.4}Co_{1-y}Fe_yO_{3-\delta}$ will cause a bending of the (Co,Fe)–O–(Co,Fe) bonds and a decrease in the bond angle below 180°. This in turn would decrease the bandwidth and cause an opening of the charge

transfer gap, resulting in a metal to semiconductor transition with increasing Fe content.

The temperature dependence of the conductivity for a semiconductor can be described by the small polaron hopping mechanism as

$$\sigma = \frac{A}{T}\exp\left(-\frac{E_a}{kT}\right) \qquad (2)$$

where $A$ is the pre-exponential factor, $T$ is the temperature, $k$ is the Boltzmann constant, and $E_a$ is the activation energy for the hopping of the small polaron. The activation energies obtained from the Arrhenius plots of $\ln(\sigma T)$ vs. $1/T$ are given in Table 1. The increase in the activation energy with $y$ in $Nd_{0.6}Sr_{0.4}Co_{1-y}Fe_yO_{3-\delta}$ implies an increase in the polaron binding energy or a decrease in the bandwidth. As discussed above, the substitution of a larger $Fe^{3+}$ for $Co^{3+}$ and the preferential formation of $Fe^{4+}$ compared to $Co^{4+}$ lead to a bending of the (Co,Fe)–O–(Co,Fe) bonds and a localization of charge carriers, which cause an increase in the polaron binding energy. Thus the decrease in bandwidth and the increase in polaron binding energy lead to an increase in the activation energy with increasing Fe doping.

The thermal expansion behaviors of $Nd_{0.6}Sr_{0.4}Co_{1-y}Fe_yO_{3-\delta}$ at 50–800 °C in air are shown in Fig. 5a. The thermal expansion behavior is related to temperature by a polynomial equation and it can be fitted as a fourth polynomial regression [21,23]. The average TEC values obtained by the fitting are plotted as a function of Fe content $y$ in Fig. 5b. The TEC value decreases with increasing Fe content $y$. A similar trend has been observed for the analogous $La_{1-x}Sr_xCo_{1-y}Fe_yO_{3-\delta}$ system [13]. A low spin $(t_{2g}^6 e_g^0)$ to high spin $(t_{2g}^4 e_g^2)$ transition associated with the $Co^{3+}$ ions as the temperature increases generally leads to a larger TEC for the $Ln_{1-x}Sr_xCoO_{3-\delta}$ system, considering the difference in the ionic radii of low spin $Co^{3+}(r=0.545$ Å) and high spin $Co^{3+}(r=0.61$ Å) ions [24,25]. It has been reported that the high spin configuration could be stabilized relative to the low spin configuration for $Co^{3+}$ by the introduction of high spin $Fe^{3+}(t_{2g}^3 e_g^2)$ in the $LaCo_{1-x}Fe_xO_3$ system [26]. Therefore, the decrease in TEC with Fe doping could be attributed to the decrease in the Co content and a suppression of the
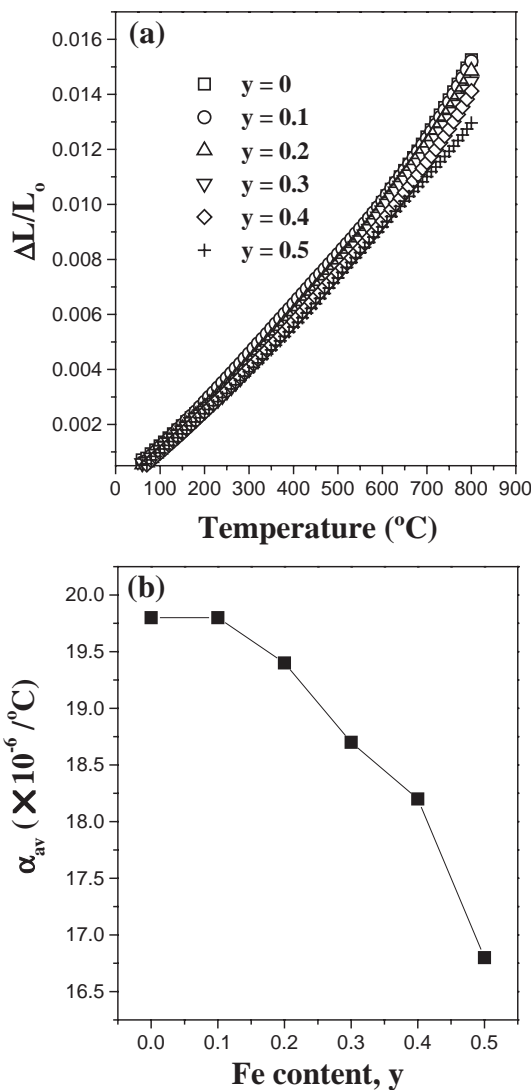


Fig. 5. Thermal expansion behaviors of $Nd_{0.6}Sr_{0.4}Co_{1-y}Fe_yO_{3-\delta}$ in air: (a) thermal expansion $(\Delta L/L_o)$ curves as a function of temperature and (b) variation of average thermal expansion coefficients $(\alpha_{AV})$ with Fe content $y$ in the temperature range of 50–800 °C.

spin state transitions associated with $Co^{3+}$. Additionally, the formation of oxygen vacancies is known to increase TEC due to a decrease in the formal oxidation state of the transition metal ions and consequent lattice expansion [27]. Since the degree of oxygen loss decreases with Fe substitution (Fig 3), it could also cause a decrease in TEC with Fe content $y$. Furthermore, TEC is inversely proportional to bonding energy between ions in the lattice [27,28]. The Fe–O bond is stronger than the Co–O bond as indicated by the TGA data (Fig. 3). Thus, the increase in bonding energy with Fe doping could also cause a decrease in TEC.

## 3.3. Electrochemical performance

The BET surface area and the average crystallite size do not vary significantly with $y$ in $Nd_{0.6}Sr_{0.4}Co_{1-y}Fe_yO_{3-\delta}$ as

Table 1
Activation energy for electrical conduction at 200–700 °C in air, BET surface area, and average crystallite size of $Nd_{0.6}Sr_{0.4}Co_{1-y}Fe_yO_{3-\delta}$

| $y$ | Activation energy[a] (eV) | BET surface area (m²/g) | Average crystallite size[b] (Å) |
|-----|---------------------------|--------------------------|----------------------------------|
| 0   | –     | 4.8 | 520 |
| 0.1 | –     | 4.0 | 600 |
| 0.2 | 0.060 | 5.0 | 460 |
| 0.3 | 0.070 | 4.9 | 460 |
| 0.4 | 0.084 | 5.2 | 450 |
| 0.5 | 0.094 | 4.2 | 580 |

[a] The error bar in the activation energy values is ±0.005 eV.
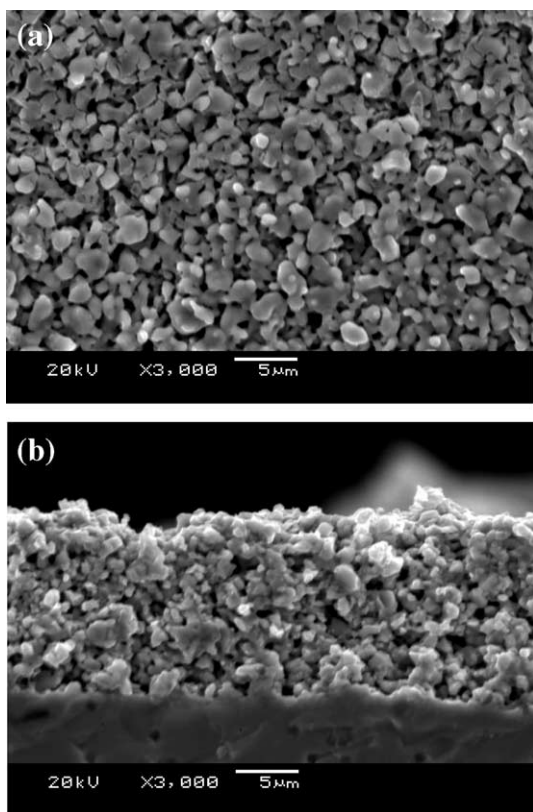[b] Average crystallite size was estimated with the line broadening of XRD peaks, and the error bar is ±10 Å.

seen in Table 1, and therefore influence of the geometrical morphology on electrochemical performance could be negligible in this study. The electrochemical performance tests were carried out with the $Nd_{0.6}Sr_{0.4}Co_{1-y}Fe_yO_{3-\delta}$/ LSGM/GDC$-$Ni single cells. Typical SEM micrographs of the top and cross-section of $Nd_{0.6}Sr_{0.4}Co_{0.7}Fe_{0.3}O_{3-\delta}$ porous cathode on LSGM electrolyte after firing at 1000 °C for 3 h are shown in Fig. 6. The grain size is about 1– 2 μm and the thickness of the cathode layer is about 10 μm. Appropriate area contact between grains and good adhesion between the cathode and electrolyte are also observed. Furthermore, the X-ray powder diffraction patterns of $Nd_{0.6}Sr_{0.4}Co_{1-y}Fe_yO_{3-\delta}$ and LSGM mixtures

Fig. 6. SEM micrographs of $Nd_{0.6}Sr_{0.4}Co_{0.7}Fe_{0.3}O_{3-\delta}$ cathode on LSGM electrolyte after firing at 1000 °C for 3 h: (a) top view and (b) cross-sectional view.



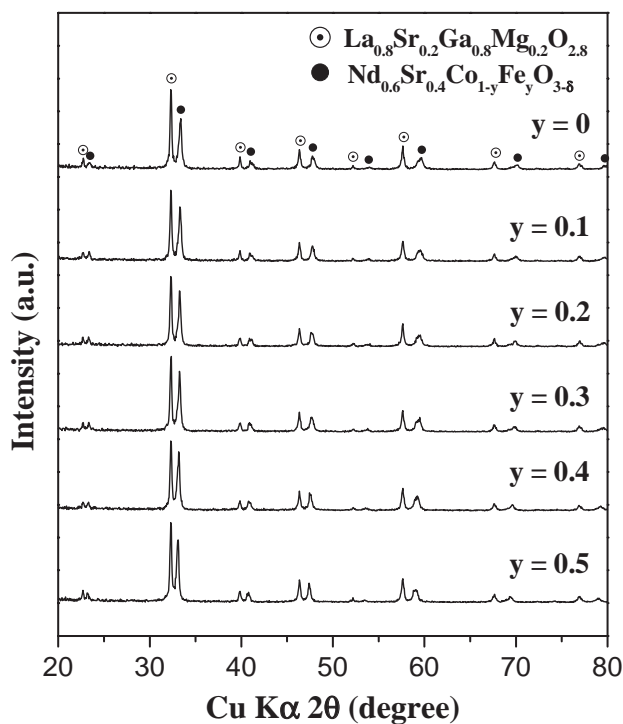Fig. 7. X-ray powder diffraction patterns recorded after heating the $Nd_{0.6}Sr_{0.4}Co_{1-y}Fe_yO_{3-\delta}$ cathode and the LSGM electrolyte powders at 1000 °C for 3 h.
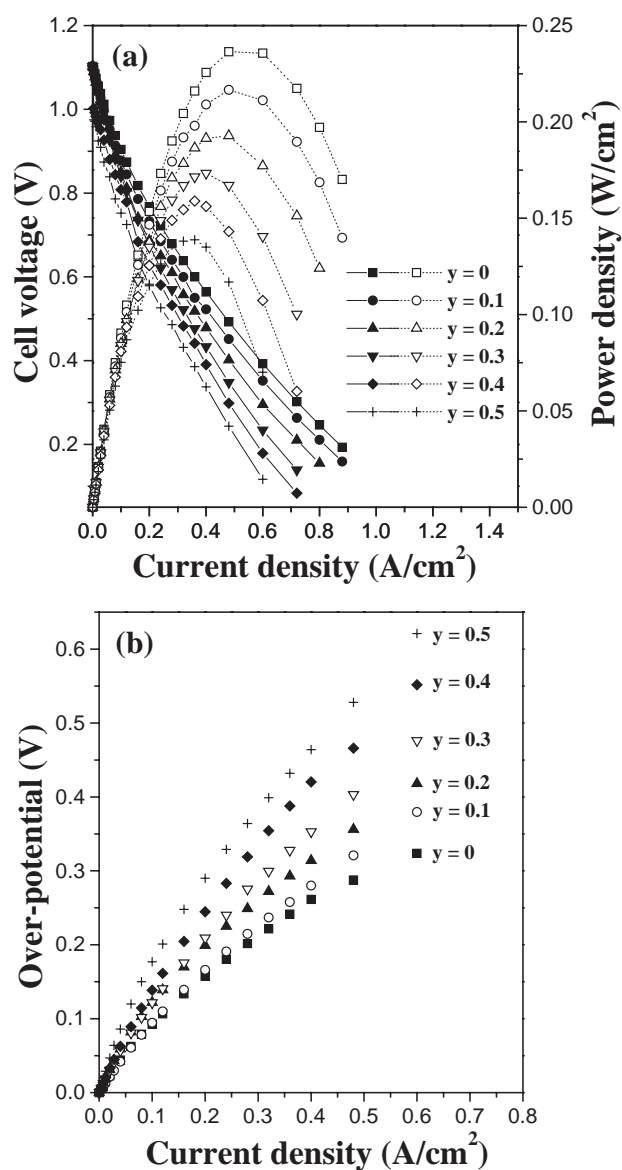


Fig. 8. Electrochemical performance data of $Nd_{0.6}Sr_{0.4}Co_{1-y}Fe_yO_{3-\delta}$/ LSGM/Ni$-$GDC single cells at 800 °C: variations of (a) the $I-V$ curve (closed symbols) and power density (open symbols) and (b) cathode over-potential.

after heating at 1000 °C for 3 h indicated no interfacial reaction for all the cathode compositions studied (Fig. 7).

The variations of the power density and the over-potential with current density at 800 °C for the various $Nd_{0.6}Sr_{0.4}Co_{1-y}Fe_yO_{3-\delta}$ cathode compositions are shown in Fig. 8. The power density decreases and the over-potential increases with increasing Fe content $y$ and the results could be understood by considering the following.

Oxygen reduction at a porous cathode is similar to a multiphase catalysis reaction that include a sequence of steps: (i) diffusion of oxygen from the gas phase $(O_{2, pore})$ to the surface of the porous cathode, (ii) dissociation of adsorbed oxygen molecule $(O_{2, ad})$ into atomic oxygen $(O_{ad})$ at the active sites, (iii) surface diffusion of oxygen atom, (iv) charge transfer; and (v) diffusion of $O^{2-}$ ions through the cathode across the cathode/electrolyte interface and into the electrolyte. Cathode over-potential is closely related not only to the charge transfer and the adsorption/dissociation of oxygen, but also to the transport speed of oxide ions through the cathode bulk and across the cathode/electrolyte interface. Therefore, the kinetics of oxygen exchange and diffusion of oxide ions in the cathode materials as well as electronic conductivity play a critical role in the oxygen reduction reaction.

The electrical conductivity decreases with increasing Fe content (Fig. 4), and the substitution of $Fe^{3+}$ for $Co^{3+}$ decreases the concentration of the oxide ion vacancies as indicated by the TGA data (Fig. 3). High oxide ion vacancy concentration in the surface of the cathode materials could improve oxygen exchange (the adsorption/dissociation of oxygen molecule) [29]. It has also been reported that the diffusion coefficient for oxygen in $La_{1-x}Sr_xCoO_{3-\delta}$ is two times higher than that in $La_{1-x}Sr_xFeO_{3-\delta}$, and the oxide ionic conductivity of $La_{1-x}Sr_xCo_{1-y}Fe_yO_{3-\delta}$ decreases with increasing Fe content [30,31]. Thus a decrease in the oxygen exchange, transport speed of oxide ions, and charge transfer kinetics resulting from a substitution of $Fe^{3+}$ for $Co^{3+}$ may lead to a decrease in the electrochemical performance.

## 4. Conclusions

Perovskite $Nd_{0.6}Sr_{0.4}Co_{1-y}Fe_yO_{3-\delta}$ $(0 \leq y \leq 0.5)$ oxides have been characterized as cathode materials for inter-mediate temperature solid oxide fuel cells. The electrical conductivity decreases with increasing Fe content due to the increased carrier localization, and the system exhibits a metal to semiconductor transition around $y = 0.2$. The thermal expansion coefficient decreases with increasing Fe content due to a suppression of the spin state transitions associated with $Co^{3+}$ and a decrease in the degree of oxygen loss at elevated temperatures. However, the Fe-doped $Nd_{0.6}Sr_{0.4}Co_{1-y}Fe_yO_{3-\delta}$ samples still have larger TEC values compared to the LSGM electrolyte. The decrease in electrical conductivity and oxide ion mobility

resulting from a decreased concentration of oxide ion vacancies leads to a decrease in electrocatalytic activity and power density with increasing Fe content. Thus, a trade-off between electrochemical performance and thermal expansion may be necessary to identify optimum cathode compositions in the Ln−Sr−Co−Fe−O system and to decrease the thermal expansion mismatch with the LSGM electrolyte.

## References

[1] M.T. Colomer, B.C.H. Steele, J.A. Kilner, Solid State Ionics 147 (2002) 41.
[2] F. Zheng, L.R. Pederson, J. Electrochem. Soc. 146 (1999) 2810.
[3] R.A. De Souza, J.A. Kilner, Solid State Ionics 106 (1998) 175.
[4] A.N. Petrov, O.F. Kononchuk, A.V. Andreev, V.A. Cherepanov, P. Kofstad, Solid State Ionics 80 (1995) 189.
[5] T. Kawada, J. Suzuki, M. Sase, A. Kaimai, K. Yashiro, Y. Nigara, J. Mizusaki, K. Kawamura, H. Yugami, J. Electrochem. Soc. 149 (2002) E252.
[6] M. Mori, Y. Hiei, N. Sammes, G.A. Tompsett, J. Electrochem. Soc. 147 (2000) 1295.
[7] Y. Takeda, H. Ueno, N. Imanishi, O. Yamamoto, N. Sammes, M.B. Phillipps, Solid State Ionics 86–88 (1996) 1187.
[8] H.Y. Tu, Y. Takeda, N. Imanishi, O. Yamamoto, Solid State Ionics 100 (1997) 283.
[9] G. Ch. Kostogloudis, N. Vasilakos, Ch. Ftikos, Solid State Ionics 106 (1998) 207.
[10] P. Shuk, V. Charton, V. Samochval, Mat. Sci. Forum 76 (1991) 161.
[11] C.H. Yo, K.S. Roh, S.J. Lee, K.H. Kim, E.J. Oh, J. Korean Chem. Soc. 35 (1991) 211.
[12] K.T. Lee, A. Manthiram, J. Electrochem. Soc. 152 (2005) A197.
[13] L.W. Tai, M.M. Nasrallah, H.U. Anderson, D.M. Sparlin, S.R. Sehlin, Solid State Ionics 76 (1995) 259.
[14] J.W. Stevenson, T.R. Armstrong, R.D. Carneim, L.R. Pederson, W.J. Weber, J. Electrochem. Soc. 143 (1996) 2722.
[15] A. Petric, P. Huang, F. Tietz, Solid State Ionics 135 (2000) 719.
[16] L.A. Chick, L.R. Pederson, G.D. Maupin, J.L. Bates, L.E. Thomas, G.J. Exarhos, Mater. Lett. 10 (1990) 6.
[17] L.V. Azaroff, Elements of X-Ray Crystallography, McGraw-Hill, New York, 1968, p. 552.
[18] R.D. Shannon, Acta Crystallogr. A32 (1976) 751.
[19] M.W. Chase Jr., C.A. Davies, J.R. Downey Jr., D.J. Frurip, R.A. McDonald, N. Syverud, J. Phys. Chem. Ref. Data 118 (Suppl. 1) (1985) 926.
[20] J. Mizusaki, Y. Mima, S. Yamauchi, K. Fueki, H. Tagawa, J. Solid State Chem. 80 (1989) 102.
[21] N. Dasgupta, R. Krishnamoorthy, K.T. Jacob, Solid State Ionics 149 (2002) 227.
[22] M.H.R. Lankhorst, J.E. ten Elshof, J. Solid State Chem. 130 (1997) 302.
[23] S.V. Chavan, S.J. Patwe, A.K. Tyagi, J. Alloy. Compd. 360 (2003) 189.
[24] K. Huang, H.Y. Lee, J.B. Goodenough, J. Electrochem. Soc. 145 (1998) 3220.
[25] M. Mori, N.M. Sammes, Solid State Ionics 146 (2000) 301.

[26] C.N.R. Rao, O.M. Parkash, P. Ganguly, J. Solid State Chem. 15 (1975) 186.

[27] H. Hayashi, M. Kanoh, C.J. Quan, H. Inaba, S. Wang, M. Dokiya, H. Tagawa, Solid State Ionics 132 (2000) 227.

[28] A.R. Ruffa, J. Mater. Sci. 15 (1980) 2258.

[29] J. Gao, X. Liu, D. Peng, G. Meng, Catal. Today 82 (2003) 207.

[30] T. Ishigaki, S. Yamauchi, K. Kishio, J. Mizusaki, K. Fueki, J. Solid State Chem. 73 (1988) 179.

[31] S. Sekido, H. Tachibana, Y. Yamamura, T. Kambara, Solid State Ionics 37 (1990) 253.